Exploring the Shape Influence on Melting Temperature, Enthalpy, and Solubility of Organic Drug Nanocrystals by a Thermodynamic Model

Gianluca Chiarappa,[†] Andrea Piccolo,[†] Italo Colombo,[†] Dritan Hasa,[‡] Dario Voinovich,[§] Mariarosa Moneghini,[§] Gabriele Grassi,[∥] Rossella Farra,[†] Michela Abrami,[∥] Paola Posocco,[†] Sabrina Pricl,[†] and Mario Grassi*[,†]

[†]Department of Engineering and Architecture, [§]Department of Chemical and Pharmaceutical Sciences, and [∥]Department of Life Sciences, Cattinara Hospital, Trieste University, Piazzale Europa 1, Trieste I-34127, Italy

[‡]Leicester School of Pharmacy, De Montfort University, The Gateway, LE1 9BH Leicester, United Kingdom

Supporting Information

ABSTRACT: This paper focuses on a thermodynamic model built to predict the reduction of organic drug melting temperature and enthalpy with nanocrystal size decrease. Indeed, this valuable information enables us to evaluate the increase of drug solubility, an aspect of paramount importance for poorly water-soluble organic drugs since a solubility increase is reflected in a bioavailability enhancement. In particular, the model considers the effect of nanocrystals shape (spherical, cylindrical, and parallelepiped-shaped) and morphology (from platelet to needle nanocrystals) on the melting temperature and enthalpy reduction with crystal size decrease. Nimesulide, a typical nonsteroidal and poorly water-soluble drug with anti-inflammatory action, has been chosen as a model drug to test model reliability. Model outcomes suggest that the reduction of melting temperature and enthalpy mainly depends on the ratio between crystals surface area and volume, i.e., on the ratio between the number of surface and bulk molecules constituting the nanocrystal network. The obtained prediction of solubility enhancement and the successful comparison with the outcomes obtained from a molecular dynamics approach, in terms of melting temperature and enthalpy decrease, have confirmed the reliability of the proposed model.

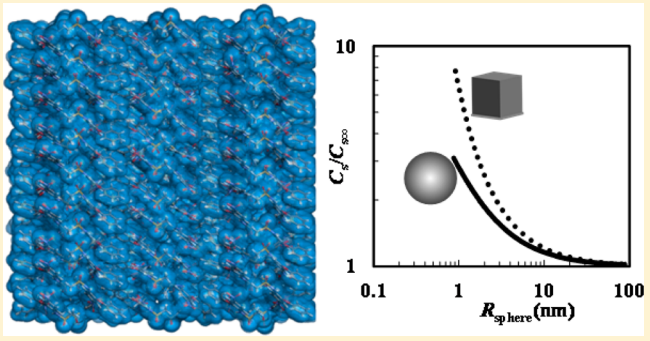

INTRODUCTION

As the oral route has always been the simplest and most appreciated way to administer drugs, many efforts were made in the past to render this way of administration also practicable for poorly water-soluble drugs which are usually characterized by low bioavailability[1] and represent approximately 40% of the drugs in the development pipelines. In addition, up to 60% of synthesized compounds are poorly soluble,[2] and 70% of potential drug candidates are discarded due to low bioavailability related to poor solubility in water.[3] Examples of commonly marketed poorly soluble drugs (water solubility less than 100 μg cm^{-3}) include analgesics, cardiovasculars, hormones, antivirals, immune suppressants, and antibiotics.[1] Thus far, an effective solution to increase the bioavailability of poorly soluble drugs has appeared to be nanonization, i.e., pulverizing solid substances into the nanometer range, which dramatically increases the crystal surface−volume ratio and the solid−liquid interface. This immediately translates into nanocrystal melting temperature (T_m) and enthalpy reduction (ΔH_m),[4] which, as a result, is reflected in the increase of drug water solubility and, in turn, drug bioavailability as discussed in the Results and Discussion.

A valid explanation for this phenomenon is the different arrangement of surface and bulk phases. In fact, surface atoms/molecules present fewer bonds than the bulk ones[5] and, accordingly, higher energy content. Therefore, surface lattice destruction necessitates less energy and is favored in comparison to the bulk one. Molecular dynamics (MD) simulation and experimental data regarding Au nanocrystals confirmed the previous theoretical analysis[6,7] by highlighting the different behavior between surface and bulk atoms. As a matter of fact, the coherent electron patterns diffracted by single nanocrystals depend on the atomic structure of surfaces. This interpretation, valid for metals, may be also extended to organic substances.[8] Indeed, the fundamentally vibrational melting entropy of organic crystals implies that organic molecules in crystalline arrangement behave analogously to

metals. This indicates that the peculiar properties of organic nanocrystals may be investigated by means of the same theoretical models employed for metallic nanocrystals. Indeed, the melting entropy of organic crystals is essentially constituted by a vibrational component, which implies that molecules in organic crystals exhibit a similarity to atoms in metallic crystals. Accordingly, for the molecular solids, the difference in activation energy between surface and bulk may be explained by a difference in molecular mobility.[8] Obviously, the surface atoms/molecules effect is macroscopically detectable only if their number is comparable to the bulk one, that is, when the surface−volume ratio is no longer negligible as it happens in nanocrystals.

Several researchers[9] investigated both experimentally and theoretically melting properties in connection with crystal size, whereas solubility dependence is still controversial due to experimental measurement difficulties.[1,10] In particular, manufacturing processes, usually altering surface characteristics by introducing lattice defects, hinder the use of fine crystals for experimental solubility determination.[11] Little impurities are able to affect solubility and polydispersed crystals experience Ostwald ripening,[12] the growth of larger crystals at the expense of the smaller ones, which leads to an asymptotic solubility diminution. Therefore, in light of these considerable experimental difficulties, the theoretical determination of drug solubility versus nanocrystals size has become mandatory. Despite the previously discussed experimental issues, the manufacturing of nanocrystal-based drug delivery systems is feasible without particular difficulties. For instance, solvent swelling,[13,14] supercritical carbon dioxide,[15,16] cogrinding,[17−21] and cryomilling[22] allow the dispersion of the drug, in the form of nanocrystals or amorphous state, inside a carrier, typically an amorphous cross-linked polymer.[23] Indeed, the polymer acts as a stabilizer for nanocrystals/amorphous drugs which, otherwise, tend to recrystallize back to their more thermodynamically stable macrocrystals status. The presence of drug and stabilizer generates a distribution of particles with different sizes, e.g., the secondary grains, which are composed of crystals, e.g., the primary grains, connected by an amorphous phase that is constituted, in turn, by the amorphous drug and/or the amorphous stabilizing agent. Furthermore, primary grains are constituted by short-range structural arrangements (crystallites) which are coherent crystalline domains, the size of which is commonly defined crystal dimension.[23] Reliability and effectiveness of such delivery systems were proved by *in vitro* and *in vivo* tests revealing considerable bioavailability improvement of poorly water-soluble but permeable drugs,[23,24] known as class II drugs according to Amidon classification.[25]

Traditionally, the peculiar properties of nanocrystals have been explored in metallurgy[26,27] and then in materials[28,29] and pharmaceutical sciences.[30] In particular, Ha and co-workers,[28] studying the crystallization of anthranilic acid (AA) in nanoporous polymer and glass matrices, were the first to report on the effect of nanoconfinement on organic polymorphic crystals. They demonstrated that polymorph selectivity during the sublimation of AA was influenced by the surface properties of glass substrates. Indeed, the preference for metastable form II in smaller pores is thought to be caused by a smaller critical nucleus size in comparison with the other two polymorphs (I and III). In another paper, Ha and co-workers,[29] examining the crystallization of organic compounds in nanochannels of controlled pore glass and porous polystyrene, detected a clear melting temperature/enthalpy depression associated with decreasing channel diameters, this being consistent with the increasing of crystals' surface/volume ratio. In addition, they realized that melting point depression also depends on the properties of the embedding matrix, and this was explained with the different nanocrystals interactions with channel walls. While Zandavi demonstrated the validity of thermodynamics at least in pores down to a radius of 1.3 nm,[31] Beiner and collaborators deepened the understanding of the effect of pores' morphology on crystals polymorphism[32] and the appearance of an amorphous drug layer between pore wall and nanocrystal surface due to drug-wall interactions.[33] Hasa and co-workers[34] and Belenguer and co-workers[35] focused the attention on cocrystals. In particular, Hasa and co-workers[34] observed how the amount of a specific liquid present during liquid-assisted mechanochemical reactions may be exploited to speedily explore polymorph diversity. Indeed, for the considered multicomponent crystalline system, formed by caffeine and anthranilic acid in a 1:1 stoichiometric ratio, only 4 of 15 liquids were found to be highly selective for one polymorphic form, while 11 of 15 produced more than one cocrystal polymorphs depending on the amount of liquid used (the selected volume range was 10−100 μL). A similar phenomenon was observed by Belenguer and co-workers,[35] by investigating two other (dimorphic) systems, namely, 1:1 theophylline/benzamide cocrystal and an aromatic disulfide compound. Importantly, Belenguer and co-workers[35] also provided a possible explanation of the reason why different amounts of a liquid produce different polymorphic forms. In fact, such phenomenon was related to particle size: polymorphs which are metastable, as micrometer-sized or larger crystals, may often be thermodynamically stabilized at the nanoscale. Additionally, surface effects were reported to be significant in polymorphism at the nanoscale and the outcomes of mechanochemical equilibrium experiments to be, in general, controlled by thermodynamics. If Lee was able to measure amorphous ibuprofen solubility resorting to nanoporous aluminum oxide,[36] Beiner and his group proved that nanoconfinement is a strategy to produce and stabilize otherwise metastable or transient polymorphs of pharmaceuticals, as required for controllable and effective drug delivery.[37,38] Myerson and co-workers[39,40] investigated the use of biocompatible alginate hydrogels as smart materials for crystallizing and encapsulating different types of drugs (acetaminophen and fenofibrate). Interestingly, they discovered that hydrogels with smaller mesh sizes appear to show faster nucleation kinetics. In addition, Myerson and co-workers[41,42] employed controlled pore glasses and porous silica supports to obtain nanocrystals of fenofibrate and griseofulvin, thus, achieving an increased dissolution rate in comparison with that of the original macrocrystals.

In the frame delineated above, the attention of this paper is devoted to nanocrystals embedded/mixed in/with an ensemble of cross-linked polymeric microparticles acting as a stabilizing agent for nanocrystals and amorphous drugs.[23] Owing to its low water solubility, good permeability, and relevance to the industrial pharmaceutical field,[1,43] nimesulide (NIM), a classical nonsteroidal anti-inflammatory drug, was selected as a proof of concept in the present study.

Thus far, the majority of theoretical approaches have been devoted to investigating the relation existing between spherical nanocrystals size and $T_m/\Delta H_m$, and only a few of them considered nonspherical shapes.[26] Moreover, they were focused on metal nanocrystals, but none of them on drug nanocrystals.

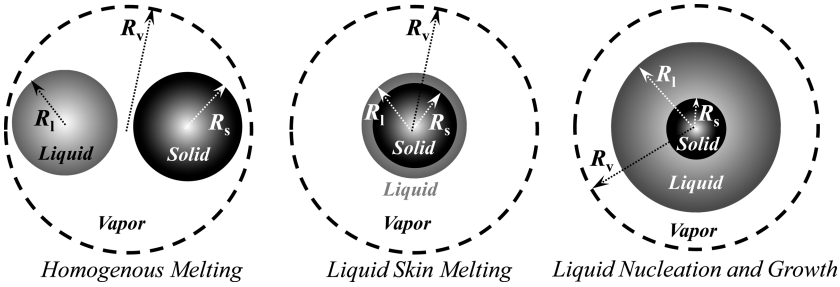

Figure 1. Thermodynamic models of nanocrystals melting are based on three mechanisms: homogeneous melting, liquid skin melting, liquid nucleation and growth. R_v, R_l, and R_s are the vapor, liquid, and solid phases radii, respectively (picture reprinted from ref 49 with permission. Copyright 2014 Croatian Society of Chemical Engineers).

To the best of our knowledge, no studies aiming at elucidating the effect of nanocrystals shape on the reduction of $T_m/\Delta H_m$ and on the consequent increase of solubility are present in the literature so far. Accordingly, this paper intends to theoretically study the dependence of $T_m/\Delta H_m$ decrease on nanocrystal size by means of a thermodynamic model distinguishing crystal shape (sphere, cylinder, parallelepiped). In addition, the outcomes of this model were validated against the corresponding $T_m/\Delta H_m$ obtained from MD calculations as a function of drug crystal shape and size.

THERMODYNAMIC MODEL

Physical Frame. At the beginning of the last century, T_m decrease by means of crystal size reduction was thermodynamically predicted and experimentally demonstrated.[44] Afterward, several researchers developed theoretical models to explain $T_m/\Delta H_m$ depression phenomenon.

Among them, the thermodynamic ones[26,45] were confirmed by MD simulations and were potentially able to describe different crystal shapes. Furthermore, these models are well adapted to describe the phenomena involved in the drug melting process. Fundamentally, thermodynamic models rely on the three physical schemes shown in Figure 1.[26] The homogeneous melting (HM) approach assumes the equilibrium between the solid and the liquid drug phases that share the same mass and lie in the vapor phase. The liquid skin melting theory (LSM) presupposes the formation of a thin liquid layer over the solid core. The thickness of the liquid layer remains constant until the solid core completely melts. According to the liquid nucleation and growth (LNG) approach, on the contrary, the liquid layer thickness grows approaching T_m. The solid core melting occurs when the liquid layer thickness is no longer negligible in comparison to the solid core size.

Despite the fact that, theoretically, there are no reasons for preferring one of the three mechanisms depicted in Figure 1 (HM, LSM, LNG), two distinct physical considerations are in favor of the LSM and LNG approaches. The first one relies on the direct observation of drug crystals melting showing the formation of a liquid shell around the solid phase before the occurrence of complete melting. The second one is strictly related to the structure of the delivery systems relying on drug nanocrystals/polymer mixtures. Indeed, regardless of the drug loading technique considered (solvent swelling, supercritical carbon dioxide, cogrinding, and cryomilling), the coexistence of drug nanocrystals and amorphous drug inside the polymeric matrix is usually observed.[46,47] Thus, when the ratio between the amount of the nanocrystalline drug and the amorphous drug is very high (i.e., when the nanocrystals mass fraction (X_{nc}) is close to one), drug melting should occur according to the physical description of the LSM approach. On the contrary, when X_{nc} approaches zero, i.e., when few nanocrystals melt inside an amorphous drug rich environment, the LNG theory appears to describe the melting process properly. Indeed, in this case, nanocrystals melting occurs in contact with a conspicuous drug liquid phase as, regardless of the nanocrystal size, melting occurs at a temperature higher than the glass transition temperature of the amorphous drug, a value over which the amorphous drug is liquid and able to flow. Accordingly, it appears reasonable to presume that, upon melting, the thickness of the liquid layer surrounding the solid core is no longer negligible in comparison to the solid core one. These considerations are based on the visual inspection of NIM crystals melting obtained by means of hot stage microscopy (see the nimesulide-melting AVI file in the Supporting Information).

Finally, as the thermodynamic model previously developed for spherical crystals[48,49] not only considers the limiting conditions $X_{nc} \to 0$ (LNG) and $X_{nc} \to 1$ (LSM), but it is also able to consider the more realistic situation $0 \le X_{nc} \le 1$, the focus of this paper is on the LSM and LNG approaches.

Mathematical Frame. Starting point is the infinitesimal, reversible variation of the internal energy, E, for closed systems composed of k components and three phases:[50]

$$dE = dE^s + dE^l + dE^v + dE^{sv} + dE^{sl} + dE^{lv} \quad (1)$$

where E^s, E^l, and E^v represent the internal energies of the solid, liquid, and vapor phases, respectively, while E^{sv}, E^{sl}, and E^{lv} are the internal energies of the solid/vapor, solid/liquid, and liquid/vapor interfaces, respectively. Beginning from eq 1, the following working equation relating the melting properties is obtainable:[48,49]

$$\Delta H_m \frac{dT_m}{T_m} = \left(\frac{1}{\rho_s} - \frac{1}{\rho_l}\right) d\left(\gamma^{lv} \frac{dA^{lv}}{dV^v}\right) - \frac{1}{\rho_s} d\left(\gamma^{sl} \frac{dA^{sl}}{dV^s}\right) \quad (2)$$

where ΔH_m is the specific melting enthalpy (J/kg), ρ_s and ρ_l are the density of the solid and liquid drug phases, respectively, γ^{lv}, γ^{sl}, A^{lv}, and A^{sl} are the surface energy and the areas of the liquid/vapor and solid/liquid interfaces, respectively, while V^v and V^s are the vapor and solid volumes, respectively. Equation 2 has to be adapted to consider the different geometrical shapes (sphere, cylinder, parallelepiped) chosen to approximate crystal shape. In particular, this adaptation regards the two derivatives dA^{lv}/dV^v and dA^{sl}/dV^s. Interstingly, assuming that ρ_s and ρ_l are equal, considering spherical crystals, regarding ΔH_m and γ^{sl} independent of temperature and curvature, respectively,

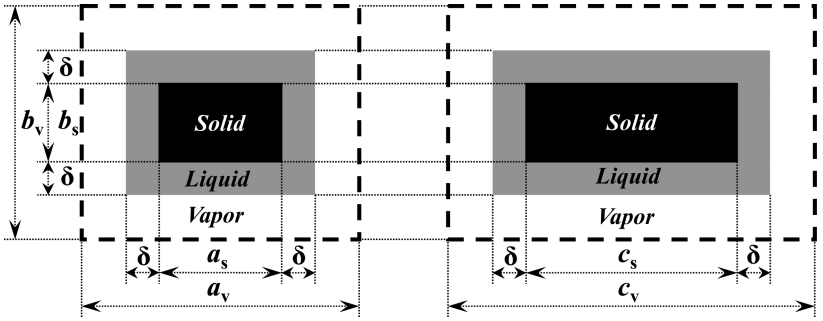

Figure 2. Spatial disposition of the three drug phases (solid, liquid, and vapor) according to the LNG and LSM theories. a_s, b_s, and c_s represent the three dimensions of the parallelepiped solid core, δ is the thickness of the surrounding liquid layer, while a_v, b_v, and c_v are the three dimensions of the vapor phase.

integration of eq 2 returns the well-known Gibbs−Thomson's equation:[29,51]

$$\frac{\Delta T_m}{T_m} = -\frac{4\gamma^{sl}}{\rho_s \Delta H_m d}\cos(\theta) \tag{3}$$

where d is crystal diameter and θ represents the contact angle of the solid nanocrystal with the pore wall in the case of crystals confined in nanopores. In the case of unconfined nanocrystals (i.e., the situation considered in this paper), $\cos(\theta) = -1$ ($\theta = 180°$).

Parallelepiped. While it is reasonable and physically sound that, in the case of a spherical crystal, the liquid phase is represented by a spherical shell (see Figure 1), the shape assumed by the liquid phase around the solid parallelepiped, on the contrary, is less obvious. However, for the sake of simplicity, it is usual to assume that the shape of the liquid phase is the same of the solid one.[52] Accordingly, Figure 2, borrowing, for a parallelepiped, the physical situation depicted in Figure 1, allows evaluation of the analytical expression of the two derivatives dA^{lv}/dV^v and dA^{sl}/dV^s:

$$\begin{aligned}\frac{dA^{lv}}{dV^v} &= \{d[2(a_s+2\delta)(b_s+2\delta)+2(a_s+2\delta)(c_s+2\delta)\\ &\quad +2(b_s+2\delta)(c_s+2\delta)]\}\\ &\quad /\{d[a_v b_v c_v-(a_s+2\delta)(b_s+2\delta)(c_s+2\delta)]\}\\ &= -\frac{4}{3a_s}\left(\frac{1}{1+2\Delta}+\frac{1}{\beta+2\Delta}+\frac{1}{\xi+2\Delta}\right)\end{aligned} \tag{4}$$

$$\frac{dA^{sl}}{dV^s} = \frac{d(2a_sb_s+2a_sc_s+2b_sc_s)}{d(a_sb_sc_s)} = \frac{4}{3a_s}\left(1+\frac{1}{\beta}+\frac{1}{\xi}\right) \tag{5}$$

where a_s, b_s, c_s, a_v, b_v, and c_v represent the three dimensions of the solid and vapor phases, respectively, δ is the thickness of the surrounding liquid layer, $\Delta = \delta/a_s$, $\beta = b_s/a_s$ and $\xi = c_s/a_s$. While performing the two derivatives, the volume $(a_v b_v c_v)$ is assumed constant.

Hence, assuming that surface energy is the same for each parallelepiped face, eq 2 becomes

$$\begin{aligned}\Delta H_m \frac{dT_m}{T_m} &= -\left(\frac{1}{\rho_s}-\frac{1}{\rho_l}\right)d\left[\gamma_\infty^{lv}\frac{4}{3a_s}\left(\frac{1}{1+2\Delta}+\frac{1}{\beta+2\Delta}\right.\right.\\ &\quad \left.\left.+\frac{1}{\xi+2\Delta}\right)\right]-\frac{1}{\rho_s}d\left[\gamma_\infty^{sl}\frac{4}{3a_s}\left(1+\frac{1}{\beta}+\frac{1}{\xi}\right)\right]\end{aligned} \tag{6}$$

where γ_∞^{lv} and γ_∞^{sl} are, respectively, the surface energy of the liquid/vapor and solid/liquid flat interfaces (infinite curvature radius). In order to evaluate the ratio Δ, it is convenient to recall the definition of X_{nc} (the ratio drug nanocrystals mass/drug total mass):

$$X_{nc} = \frac{\rho_s a_s b_s c_s}{\rho_s a_s b_s c_s + \rho_l[(a_s+2\delta)(b_s+2\delta)(c_s+2\delta)-a_s b_s c_s]} \tag{7}$$

Equation 7 inversion allows the determination of the function $\Delta(X_{nc})$:

$$\Delta^3 + \frac{1+\beta+\xi}{2}\Delta^2 + \frac{\beta+\beta\xi+\xi}{4}\Delta + \frac{\beta\xi\rho_s}{8\rho_l}\left(1-\frac{1}{X_{nc}}\right) = 0 \tag{8}$$

The numerical solution of eq 7 (Newton's method) enables the evaluation of the parameter Δ required by eq 6. It is clear that $\Delta \to \infty$ in the case $X_{nc} \to 0$ (LNG), while $\Delta \to 0$ when $X_{nc} \to 1$ (LSM). In the real case, $0 \le X_{nc} \le 1$, obviously $0 \le \Delta < \infty$. While eq 7 strictly applies to monodispersed nanocrystals, it also holds, on average, for polydispersed ones.

Assuming both ρ_s and ρ_l constant and independent of a_s, the integration of eq 6 from the melting temperature of the infinitely large crystal ($T_{m\infty}$) to the melting temperature of the nanocrystal with size a_s (T_m), allows finding the working equation holding for parallelepipeds:

$$\begin{aligned}\int_{T_{m\infty}}^{T_m}\Delta H_m\frac{dT_m}{T_m} &= -\frac{4}{3a_s}\left[\gamma_\infty^{lv}\left(\frac{1}{\rho_s}-\frac{1}{\rho_l}\right)\left(\frac{1}{1+2\Delta}\right.\right.\\ &\quad \left.\left.+\frac{1}{\beta+2\Delta}+\frac{1}{\xi+2\Delta}\right)+\frac{\gamma_\infty^{sl}}{\rho_s}\left(1+\frac{1}{\beta}+\frac{1}{\xi}\right)\right]\end{aligned} \tag{9}$$

Implicitly, eq 9 implies that surface energy (both γ_∞^{lv} and γ_∞^{sl}) is independent of crystal shape (β, ξ), dimension (a_s) and crystal facet. As a matter of fact, this assumption is sometimes unverified, as nicely documented by Heng and co-workers,[53] who proved that paracetamol form I crystals exhibit different surface energies on distinct crystal facets. In this particular case,

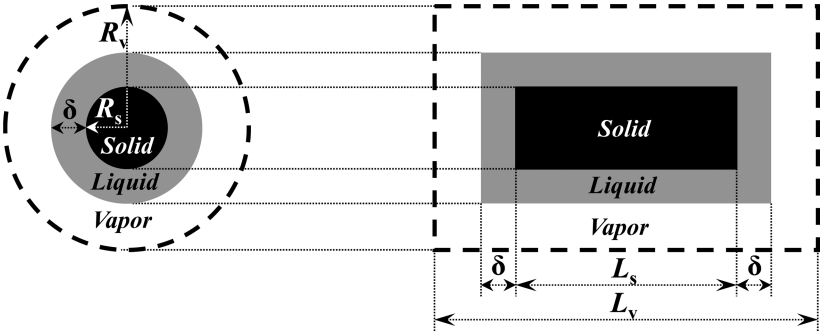

Figure 3. Spatial disposition of the three drug phases (solid, liquid, and vapor) according to the LNG and LSM theories. R_s and L_s represent the radius and the length of the cylinder solid core, respectively, δ is the thickness of the surrounding liquid layer, while R_v and L_v are the radius and the length of the vapor phase, respectively.

the explanation for this occurrence was the variable number of hydroxyl groups present on crystal facets. It is worth mentioning that, in principle, the derivation of eq 9 could also consider surface energy dependence on crystal shape, dimension, and facet. In particular, in order to take account of surface energy dependence on crystal facet, eq 9 modification is relatively straightforward provided that the surface energy pertaining to each facet is available.

In order to solve eq 9 and obtain T_m dependence on a_s, it is necessary to evaluate ΔH_m dependence on T_m (see the integral in eq 9). In this context, the classic thermodynamic approach employed by Zhang and co-workers, holding regardless of nanocrystal nature (organic or inorganic) and being characterized by easily determinable parameters, may be considered.[9] This approach relies on a thermodynamic cycle according to which ΔH_m is the sum of five different contributions. The first is due to the aggregation of nanoparallelepipeds with size a_s into the bulk phase at the nanocrystals melting temperature T_m (ΔH_1). The second implies the bulk phase heating from T_m to the infinitely large crystal melting temperature $T_{m\infty}$ (ΔH_2), while the third represents the bulk phase melting at $T_{m\infty}$ (ΔH_3). The fourth implies the bulk liquid disintegration into liquid nanoparallelepipeds with size a_s at $T_{m\infty}$ (ΔH_4) and, finally, the fifth is the cooling of the liquid particles from $T_{m\infty}$ to the nanocrystals melting temperature T_m (ΔH_5):

$$\begin{aligned}\Delta H_m &= \left[-\gamma_\infty^{sv}\frac{A^{sv}}{\rho_s V^s}\right]_{(1)} + \left[\int_{T_m}^{T_{m\infty}} C_P^s dT\right]_{(2)} + [\Delta H_{m\infty}]_{(3)} \\ &\quad + \left[\gamma_\infty^{lv}\frac{A^{lv}}{\rho_l V^l}\right]_{(4)} + \left[\int_{T_{m\infty}}^{T_m} C_P^l dT\right]_{(5)} \\ &= \Delta H_{m\infty} - \frac{2}{a_s}\left(\frac{\gamma_\infty^{sv}}{\rho_s} - \frac{\gamma_\infty^{lv}}{\rho_l}\right)\left(1 + \frac{1}{\beta} + \frac{1}{\xi}\right) \\ &\quad - (C_P^l - C_P^s)(T_{m\infty} - T_m)\end{aligned} \tag{10}$$

where $\Delta H_{m\infty}$ is the specific melting enthalpy (J/kg) of an infinitely large crystal, V^s and A^{sv} are, respectively, the solid phase volume and the area of the solid−vapor interface referring to the ensemble of parallelepipeds with dimensions a_s, b_s, c_s, V^l, and A^{lv} are, respectively, the liquid phase volume and the area of the liquid−vapor interface referring to the ensemble of parallelepipeds with dimensions a_s, b_s, c_s, γ_∞^{sv}, and γ_∞^{lv} are the surface energy of the plane solid/vapor and liquid/vapor interfaces, respectively, while C_P^s and C_P^l are the solid and liquid drug specific heat capacities at constant pressure (J/kg K), respectively, whose difference is almost constant and temperature independent.[48]

The melting properties dependence on nanoparallelepipeds size a_s ($T_m(a_s)$; $\Delta H_m(a_s)$) is achieved by the simultaneous numerical solution of eq 9 and eq 10 (see Appendix for details).

Cylinder. Following the same strategy adopted for parallelepipeds, the two derivatives dA^{lv}/dV^v and dA^{sl}/dV^s become, for cylindrical crystals (see Figure 3):

$$\begin{aligned}\frac{dA^{lv}}{dV^v} &= \frac{d[2\pi(R_s+\delta)^2 + 2\pi(R_s+\delta)(L_s+2\delta)]}{d[\pi R_v^2 L_v - \pi(R_s+\delta)^2(L_s+2\delta)]} \\ &= -\frac{4}{3R_s}\left(\frac{1}{1+\Delta} + \frac{1}{\lambda+2\Delta}\right)\end{aligned} \tag{11}$$

$$\frac{dA^{sl}}{dV^s} = \frac{d(2\pi R_s^2 + 2\pi R_s L_s)}{d(\pi R_s^2 L_s)} = \frac{4}{3R_s}\left(1 + \frac{1}{\lambda}\right) \tag{12}$$

where $\Delta = \delta/R_s$ and $\lambda = L_s/R_s$. While performing the two derivatives, the volume $\pi R_v^2 L_v$ is assumed constant.

For cylindrical crystals, particular attention has to be paid to the expression of the interface energy as, while assuming the lateral surface of the cylinder chemically and physically equal to the two bases, the different curvature of the bases (infinite curvature) and the lateral surface (curvature = $1/R_s$) have to be considered. Indeed, it is well-known that surface energy depends on surface curvature according to the following equation:[54−57]

$$\frac{\gamma}{\gamma_\infty} = \left(1 + \frac{2\delta_0}{r}\right)^{-1} \tag{13}$$

where γ and γ_∞ are the energy of a surface with curvature radius r and that of a flat surface (infinite curvature radius), respectively, while δ_0 is Tolman's length whose order of magnitude should correspond to the actual diameter (d_m) of the molecules constituting the bulk phase, and it is usually assumed to be $d_m/3$.[58] Equation 13 predicts that surface energy tends toward zero for low values of r. Hence, according to eqs 11−13, eq 2 becomes

$$\int_{T_{m\infty}}^{T_m} \Delta H_m \frac{dT_m}{T_m} = -\left(\frac{1}{\rho_s} - \frac{1}{\rho_l}\right) d\left\{\gamma_\infty^{lv} \frac{4}{3}\left[\frac{1}{R_s(1+\Delta)+2\delta_0} + \frac{1}{R_s(\lambda+2\Delta)}\right]\right\} - \frac{1}{\rho_s} d\left[\gamma_\infty^{sl} \frac{4}{3}\left(\frac{1}{R_s+2\delta_0} + \frac{1}{\lambda R_s}\right)\right] \quad (14)$$

Also in this case, Δ may be evaluated resorting to X_{nc}:

$$X_{nc} = \frac{\rho_s \pi R_s^2 L_s}{\rho_s \pi R_s^2 L_s + \rho_l[\pi(R_s+\delta)^2(L_s+2\delta) - \pi R_s^2 L_s]} \quad (15)$$

or

$$\Delta^3 + \left(2 + \frac{\lambda}{2}\right)\Delta^2 + (\lambda+1)\Delta + \frac{\lambda\rho_s}{2\rho_l}\left(1 - \frac{1}{X_{nc}}\right) = 0 \quad (16)$$

The numerical solution (Newton's method) of eq 16 allows determining the parameter Δ required by eq 14. Assuming both ρ_s and ρ_l independent of R_s, the integration of eq 14 from the melting temperature of the infinitely large crystal ($T_{m\infty}$) to the one of the nanocrystal with radius R_s (T_m) allows finding the working equation holding for cylinders:

$$\int_{T_{m\infty}}^{T_m} \Delta H_m \frac{dT_m}{T_m} = -\frac{4}{3}\left\{\gamma_\infty^{lv}\left(\frac{1}{\rho_s} - \frac{1}{\rho_l}\right)\left[\frac{1}{R_s(1+\Delta)+2\delta_0} + \frac{1}{R_s(\lambda+2\Delta)}\right] + \frac{\gamma_\infty^{sl}}{\rho_s}\left(\frac{1}{R_s+2\delta_0} + \frac{1}{\lambda R_s}\right)\right\} \quad (17)$$

Also in this case, eq 17 solution requires the evaluation of ΔH_m on T_m (see the integral in eq 17) and Zhang's approach may be used.[9] For cylinders, it reads:

$$\Delta H_m = \left[-\gamma_\infty^{sv}\frac{A^{sv}}{\rho_s V^s}\right]_{(1)} + \left[\int_{T_m}^{T_{m\infty}} C_P^s dT\right]_{(2)} + [\Delta H_{m\infty}]_{(3)} + \left[\gamma_\infty^{lv}\frac{A^{lv}}{\rho_l V^l}\right]_{(4)} + \left[\int_{T_{m\infty}}^{T_m} C_P^l dT\right]_{(5)}$$
$$= \Delta H_{m\infty} - 2\left(\frac{\gamma_\infty^{sv}}{\rho_s} - \frac{\gamma_\infty^{lv}}{\rho_l}\right)\left(\frac{1}{\lambda R_s} + \frac{1}{R_s+2\delta_0}\right) - (C_P^l - C_P^s)(T_{m\infty} - T_m) \quad (18)$$

where V^s and A^{sv} are the solid phase volume and the area of the solid–vapor interface referring to the ensemble of cylinders with radius R_s and length L_s, respectively, while V^l and A^{lv} are the liquid phase volume and the area of the liquid–vapor interface referring to the ensemble of cylinders with radius R_s and length L_s, respectively. Equation 17–18 inspection reveals that the reduction of surface energy (γ^{lv}, γ^{sl}) with cylinder radius (see eq 13) implies a smaller decrease of both ΔH_m and T_m.

The melting properties dependence on nanocylinders radius R_s ($T_m(R_s)$; $\Delta H_m(R_s)$) is achieved by the simultaneous numerical solution of eq 17 and eq 18 (see Appendix for details).

MOLECULAR DYNAMICS CALCULATIONS

Because of the intrinsic difficulties in obtaining $T_m/\Delta H_m$ of specific sized and shaped nanocrystals from experimental tests, in the present work, we resorted to MD calculations in order to evaluate the aforementioned properties. Atomistic MD simulations explicitly represent atoms constituting a nanocrystal; as a consequence, $T_m/\Delta H_m$ calculation may become computationally unfeasible especially for large crystals. In the present study, reference model volumes were selected as the best compromise between the computational time required to accurately derive $T_m/\Delta H_m$ and the values needed for the comparison with the thermodynamic model. The minimum simulated volume in each data set ensures the construction of a reliable nanocrystal molecular model featuring at least three crystallographic units in each direction whatever the nanocrystal shape and shape ratio.

The NIM single crystal structure was retrieved from the Cambridge Structural Database (Cambridge, UK) (CCDC 773602).[59] NIM orthorhombic $Pca2_1$ crystal cell parameters are the following: a 16.1268 Å, b 5.0411 Å, c 32.761 Å, α 90°, β 90°, γ 90°.

Crystal cell was optimized by using the Dreiding force field with charges derived by fitting the electrostatic potential surface of the optimized structure at the B3LYP/6-31G (d,p) level by Turbomole 7.1 (http://www.turbomole-gmbh.com) and RESP method.[60,61] Single crystal NIM nanoparticles (NPs) of appropriate dimensions and shape were built by employing the *Nanocluster* module present in Materials Studio v. 6.1 (Accelrys Inc., USA) program (http://accelrys.com/products/collaborative-science/biovia-materials-studio/). Free boundary conditions (free surfaces with vacuum) were applied for MD simulations, which were performed within the canonical ensemble (NVT) where a constant temperature T was maintained by using the Berendsen method in a constant volume V.[62] van der Waals and electrostatic interactions were modeled by using a Lennard–Jones potential and a group based summation method, respectively, truncated at 1.20 nm. A 1 fs time step was used throughout the simulations. NIM NPs were first relaxed at 300 K for 1 ns before heating, which was gradually applied by increasing the NP temperature in intervals. Then, the NPs were equilibrated for at least 15 ns at each temperature taking the last phase space point of a calculation as an input for the next temperature calculation. The MD simulations were run by Materials Studio v. 6.1 software in an in-house cluster.

Nanocrystals T_m was evaluated by calculating the potential energy per NIM molecule (at each temperature, the potential energy was averaged over the last 5 ns of each simulation with at least 500 independent configurations) upon heating, and then determining the melting point as the temperature where the potential energy changes abruptly, at the first-order transition point. In addition, ΔH_m could be calculated with the associated increment of the potential energy.

The computational procedure described above was also applied to two further drug crystal models, namely, Nifedipine (NIF) and Griseofulvin (GRI). The unit cell of NIF structure (CCDC BICCIZ) has the following properties: monoclinic $P1$, a 10.923 Å, b 10.326 Å, c 14.814 Å, α 90°, β 92.7°, γ 90°. GRI (CCDC GRISFL02) has a tetragonal cell and a $P41$ space group with lattice parameters: a 8.967 Å, b 8.967 Å, c 19.904 Å,

α 90°, β 90°, γ 90°. The COMPASS force field[63,64] was applied for these molecular dynamics simulations with charged calculated at B3LYP/6-31G(d) level.

RESULTS AND DISCUSSION

In order to understand the effect of geometry on the considered nanocrystals thermal properties, it is useful to recall the working equations holding for spherical crystals:[48,49]

$$\int_{T_{m\infty}}^{T_m} \Delta H_m \frac{dT_m}{T_m} = -2\left[\left(\frac{1}{\rho_s} - \frac{1}{\rho_l}\right)\frac{\gamma_\infty^{lv}}{\alpha R_s + 2\delta_0} + \frac{\gamma_\infty^{sl}}{\rho_s(R_s + 2\delta_0)}\right] \quad \alpha = \sqrt[3]{1 + \frac{\rho_s}{\rho_l}\left(\frac{1}{X_{nc}} - 1\right)} \tag{19}$$

$$\Delta H_m = \Delta H_{m\infty} - \frac{3}{R_s + 2\delta_0}\left(\frac{\gamma_\infty^{sv}}{\rho_s} - \frac{\gamma_\infty^{lv}}{\rho_l}\right) - (C_P^l - C_P^s)(T_{m\infty} - T_m) \quad \text{Zhang's equation} \tag{20}$$

To perform a sound comparison among the thermal properties of differently shaped crystals, it is no longer possible to refer to sphere radius (R_s), parallelepiped base side (a_s) and cylinder base radius (R_s). Indeed, in so doing, we would compare T_m and ΔH_m of crystals having different volumes and, thus, different masses. As melting is a bulk phenomenon (although it starts from the surface), the comparison of the thermal properties have to be referred to nanocrystals characterized by equal volume V_C (sphere $4\pi R_s^3/3$; parallelepiped $a_s b_s c_s$; cylinder $\pi R_s^2 L_s$) and, consequently, different R_s and a_s. Accordingly, eqs 9−10, 17−18, and 19−20 were solved as functions of a_s (parallelepiped), R_s (cylinder), and R_s (sphere), respectively. Knowing T_m(a_s or R_s) and ΔH_m(a_s or R_s), it was, then, possible to develop and compare the corresponding trends $T_m(V_C)$ and $\Delta H_m(V_C)$ for the three different considered geometries. Model features were explored by considering NIM, a drug belonging to the Amidon's class II (poorly water-soluble but permeable drug)[25] as a proof of concept. Its physicochemical characteristics[48,65] are summarized in Table 1.

Figure 4, showing T_m and ΔH_m depression in the case of parallelepiped-shaped crystals characterized by X_{nc} = 1 and a square basis ($\beta = a_s/b_s = 1$), clarifies the effect of the shape ratio ξ (= c_s/a_s) (the representation is inferiorly limited to the volume of approximately four NIM unit cells ≈11 nm^3). It is observable that the shape ratio ξ affects in a qualitatively similar manner both T_m and ΔH_m, even if its effect appears more accentuated for T_m. In particular, Figure 4 shows that, at fixed crystal volume (V_C), platelet nanocrystals (ξ = 0.01) are characterized by lower T_m and ΔH_m than rod-shaped (ξ = 100) nanocrystals. In addition, both of them show lower T_m and ΔH_m than cubic nanocrystals. Conversely, at fixed T_m or ΔH_m, cubic crystals are characterized by the smallest dimensions among the other shapes (rods and platelets). It is worth mentioning that the relation existing between T_m and V_C is substantially compatible with the outcomes of nucleation theory, which allows determining the size (V_C) of the smallest nucleus (namely, a cluster of molecules) which a crystal originates from.[30]

This model output is explicable remembering what was observed by Magomedov[66,67] and presented in the introduction, i.e., the importance of the ratio between the surface and bulk molecules. Indeed, at constant volume (V_C), cubic crystals show the minimum surface−volume ratio with respect to the other conformations (rods and platelets), as witnessed by eq 21 and Figure 5:

$$\frac{a_c}{2}\frac{A^s}{V^s} = \sqrt[3]{\beta}\left[\sqrt[3]{\frac{1}{\xi^2}} + \sqrt[3]{\xi}\left(1 + \frac{1}{\beta}\right)\right] \tag{21}$$

where a_c stands for the side of the cube, while A^s and V^s (= V_C = $a_c b_c c_c$) are the surface and the volume of the crystal, respectively. Additionally, the higher surface−volume ratio shown by the platelet crystals with respect to rod crystals (Figure 5) explains why platelet crystals are characterized by lower T_m and ΔH_m in comparison to rod crystals.

Table 1. Nimesulide Physicochemical Parameters[a]

formula	$C_{13}H_{12}N_2O_5S$	ref
UCS (nm)	1.74	59
M_w (−)	308.51	43
γ_∞^{sl} (J/m^2)	0.0133	21
γ_∞^{lv} (J/m^2)	0.0433	21
γ_∞^{sv} (J/m^2)	0.0576	21
δ_0 (nm)	0.2385	21
ρ_s (kg/m^3)	1490.0	21
ρ_l (kg/m^3)	1343.7	21
$T_{m\infty}$ (°C)	148.7	21
$\Delta H_{m\infty}$ (J/kg)	108720	21
ΔC_P (J/kg °C)	333.3	21
V_m (m^3/mol)	192 × 10^{-6}	21
C_s (μg/cm^3) - 37 °C, pH 1.2	11.8 ± 0.5	65
C_s (μg/cm^3) - 37 °C, pH 7.5	104 ± 12	65

[a]UCS indicates the diameter of the unit cell imagined as a sphere, M_w is the molecular weight, γ_∞^{sl}, γ_∞^{lv}, and γ_∞^{sv} are, respectively, the solid−liquid, liquid−vapor, and solid−vapor surface energy referring to a plane surface (infinite curvature radius), δ_0 is the Tolman's length, ρ_s and ρ_l are, respectively, the solid and the liquid densities, $T_{m\infty}$ and $\Delta H_{m\infty}$ are, respectively, the melting temperature and enthalpy of the infinitely large crystal, ΔC_P is the difference between the liquid and the solid specific heat at constant pressure, V_m is the molar volume, while C_s is the solubility in water (37°C).

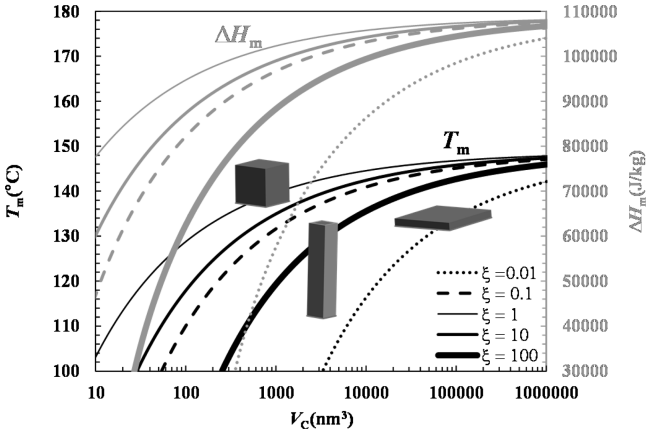

Figure 4. Effect of the shape ratio $\xi = c_s/a_s$ on the melting temperature T_m (left vertical axis, black lines) and enthalpy ΔH_m (right vertical axis, gray lines) of parallelepiped-shaped nanocrystals, assuming the nanocrystals mass fraction X_{nc} = 1 and $\beta = a_s/b_s = 1$. a_s, b_s, and c_s are the dimensions of the parallelepiped-shaped crystal, while V_C is the crystal volume. The shaded parallelepipeds qualitatively represent the shape of the crystals pertaining to the curve they intersect.

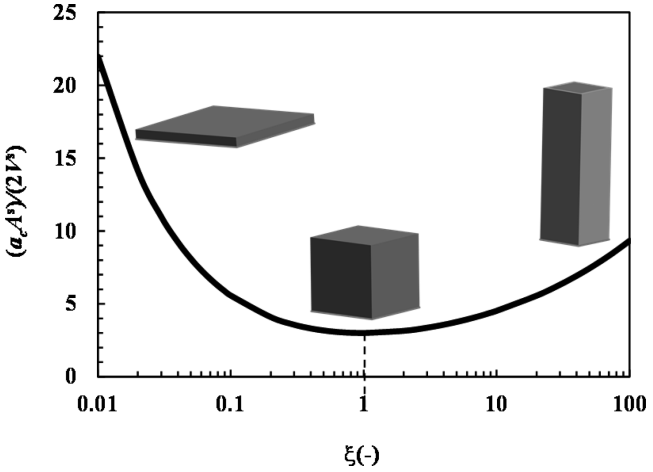

Figure 5. Equation 21 plot showing the dependence of the dimensionless ratio between crystal surface (A^s) and volume (V^s) on the shape ratio $\xi = c_s/a_c$ at constant volume. The value $\beta = b_s/a_c = 1$ was assumed to perform a coherent connection with Figure 4. The shaded parallelepipeds qualitatively represent the shape of the crystals pertaining to the different ξ values.

In the case of cylindrical crystals, model results (eqs 17−18) are qualitatively similar to those found for parallelepipeds. Indeed, Figure 6, showing the effect of the shape ratio λ on T_m

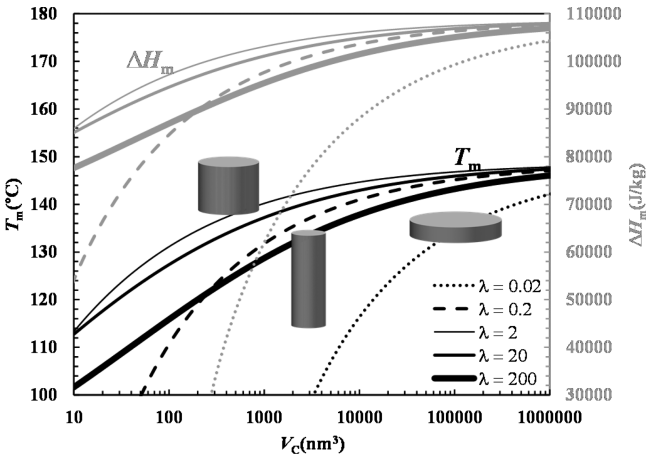

Figure 6. Effect of the shape ratio $\lambda = L_s/R_s$ on the melting temperature T_m (left vertical axis, black lines) and enthalpy ΔH_m (right vertical axis, gray lines) of cylindrical nanocrystals assuming the nanocrystals mass fraction $X_{nc} = 1$. L_s and R_s are the length and the radius of the cylindrical-shaped crystal, while V_C is the crystal volume. The shaded cylinders qualitatively represent the shape of the crystals pertaining to the curve they intersect.

and ΔH_m depression, reveals that rod-shaped ($\lambda = 200$; black/gray solid thickest lines) and platelet-shaped ($\lambda = 0.02$; black/gray dotted lines) crystals are characterized by more consistent reductions of T_m and ΔH_m than those referring to the equilateral cylinder ($\lambda = 2$; black/gray solid thinnest lines) (the representation is inferiorly limited to the volume of approximately four NIM unit cells ≈ 11 nm^3). However, since the surface−volume ratio of the equilateral cylinder is not so far from that of the rod-shaped crystals (see Figure 7 and eq 22):

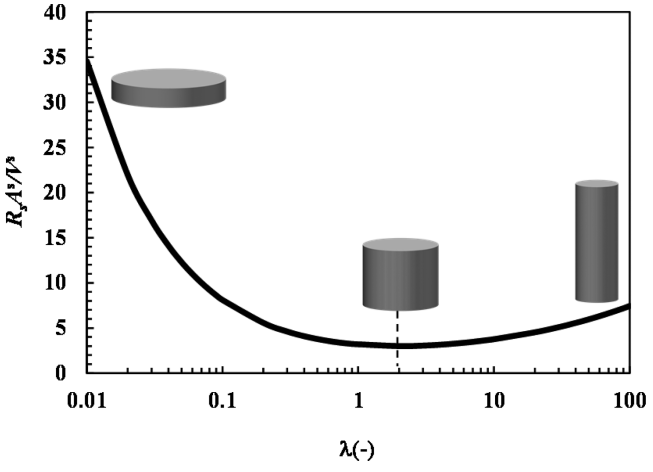

Figure 7. Equation 22 plot showing the dependence of the dimensionless ratio between crystal surface (A^s) and volume (V^s) on the shape ratio $\lambda = L_s/R_s$ at constant volume. The shaded cylinders qualitatively represent the shape of the crystals pertaining to the different λ values.

$$\frac{A^s R_s}{V^s} = \sqrt[3]{\frac{4}{\lambda^2}} + \sqrt[3]{4\lambda} \tag{22}$$

T_m and ΔH_m trends of the rod-shaped crystals are not so clearly detached from those of the equilateral one as in the case of parallelepiped-shaped crystals (Figure 4).

It is important to remind that the value of X_{nc} appears not to heavily affect the results shown in Figure 4 and Figure 6, where $X_{nc} = 1$ was considered.

It is now interesting to evaluate the effect of nanocrystals shape (sphere, cube ($\xi = \beta = 1$) and equilateral cylinder ($\lambda = 2$)) on the T_m and ΔH_m depression. Figure 8, concerning the melting process of spherical, cubic, and (equilateral) cylindrical crystals, clarifies that, at equal crystal volume (V_C), T_m and ΔH_m of cubic nanocrystals are lower than those of cylindrical nanocrystals. In turn, cylindrical nanocrystals show lower T_m and ΔH_m with respect to spherical nanocrystals. The

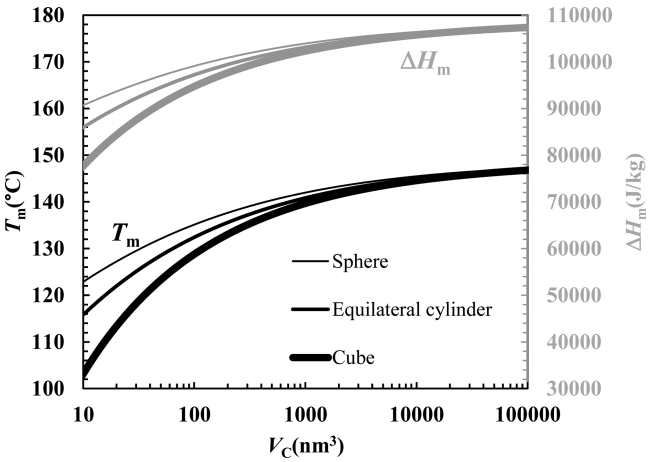

Figure 8. Effect of geometry (sphere, cube ($\xi = \beta = 1$), equilateral cylinder ($\lambda = 2$)) on the melting temperature T_m (left vertical axis, black lines) and enthalpy ΔH_m (right vertical axis, gray lines) depression assuming the nanocrystals mass fraction $X_{nc} = 1$. The representation is inferiorly limited to the volume of approximately four nimesulide unit cells ≈ 11 nm^3.

explanation of this behavior relies on both the dimensionless surface-volume ratio (cube → 3; equilateral cylinder → 2; sphere → 3) and the reduction of surface energy with surface curvature ($1/r$, see eq 13). Indeed, not only cubic crystals are characterized by the highest value of the surface−volume ratio, but they also show the highest surface energy as they are constituted by plane surfaces (curvature = $1/r \rightarrow 0$).

On the contrary, spherical crystals, although characterized by the same surface−volume ratio (3), suffer from the reduction of surface energy with curvature, this last one increasing as crystal radius decreases. Equation 2 clarifies that, for vanishing values of γ^{lv} and γ^{sl}, T_m and ΔH_m are independent of sphere radius. Cylindrical crystals are in between the spherical and cubic ones as they are characterized by the smallest surface−volume ratio, but the effect of curvature affects only the lateral surface and not the two bases.

The findings of this paper are reflected in two crucial and practical aspects characterizing the nanocrystals based delivery systems, i.e., the nanocrystals size distribution inside the polymeric carrier and nanocrystals water solubility.

For this purpose, it is useful to consider a system made by cogrinding, for 1 h, NIM and cross-linked polyvinylpyrrolidone (PVP) in a mass ratio 1:3.[21] Relying on the presented model, on the differential scanning calorimetry (DSC) characterization and the theoretical strategy performed by Coceani and co-workers,[21] it is possible to evaluate the nanocrystals size distribution of the considered NIM−PVP system. To perform a more significant analysis of the geometry effects, it is convenient to express the nanocrystals size distribution ($f(1/\text{nm})$) as a function of the radius, R_{sphere}, of the equivalent sphere sharing the same volume of the considered crystal. The inspection of Figure 9 reveals that both distribution wideness

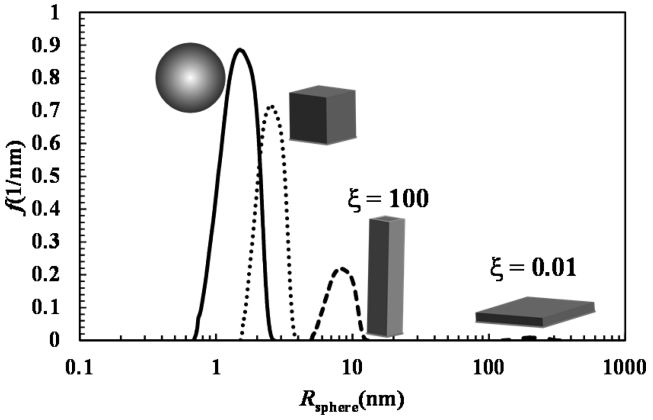

Figure 9. Effect of nanocrystals geometry (sphere, cube ($\xi = \beta = 1$) and parallelepiped ($\xi = 0.01$ and 100; $\beta = 1$)) on their size distribution (f) referring to the nimesulide−polyvinylpyrrolidone (1:3) system described in ref 21. R_{sphere} is the radius of the equivalent sphere sharing the same volume of the parallelepiped-shaped nanocrystals. Nimesulide unit cell half dimension corresponds to R_{sphere} = 0.77 nm.

and peak position increase when considering, in order, spherical, cubic, and parallelepiped (rods $\beta = 1$ and $\xi = 100$; platelets $\beta = 1$ and $\xi = 0.01$) nanocrystals. This result sounds reasonable as, in the case of spherical crystals, the size distribution lies very close to the physical limit of NIM nanocrystals, i.e., one-half of NIM unit cell (0.77 nm). On the contrary, when cubic nanocrystals are considered (whose shape is close to that of the real NIM crystals as predicted by the WinXMorph software[68]), the distribution moves toward larger radii. Finally, increasingly larger radii are considered by the rod and platelet distributions. These findings could contribute to explain why, presuming crystals to be spherical, the determination of crystals size by DSC is usually lower than that performed by means of the X-ray approach.[48,69]

Moving to the effect of geometry on nanocrystals water solubility, it is useful to recall the relation existing between solubility and T_m or ΔH_m:[48]

$$X_d = \frac{1}{\gamma_d}\left(\frac{T}{T_m}\right)^{\Delta c_p/R} \exp\left\{-\left[\frac{\Delta h_m}{RT}\left(1 - \frac{T}{T_m}\right) + \frac{\Delta c_p}{R}\left(1 - \frac{T_m}{T}\right)\right]\right\} \quad C_s = \frac{X_d}{1 - X_d}\frac{M_d}{M_s}\rho_{sol} \tag{23}$$

where X_d is the drug molar solubility, γ_d is the drug activity coefficient, Δh_m and Δc_p are, respectively, the drug molar melting enthalpy and the difference between the solid (drug) and the liquid (drug) molar specific heat at constant pressure, M_d and M_s are, respectively, the drug and the solvent molecular weight, ρ_{sol} is the solvent density, R is the universal gas constant, while C_s is the mass/volume nanocrystal solubility. Equation 23 derives from the classical theory of thermodynamic equilibrium between a solid phase (of component "1") and a liquid one (of component "2") assuming, as commonly done, that only the solid component (1) is able to spread between the solid and the liquid phase (i.e., the liquid phase is unable to dissolve in the solid crystalline network). Equating the fugacity of compound "1" in the solid and the liquid phase, eq 23 is obtained. This thermodynamic approach leads to the interesting conclusion that the solubility of "1" in the liquid phase also depends on T_m and the molar melting enthalpy (Δh_m) of the solid phase. In particular, the lower T_m and Δh_m, the higher the solubility of the solid phase in the liquid one, as witnessed by Figure 10 that depicts eq 23 outcomes concerning the solubility trend of spherical and cubic NIM nanocrystals

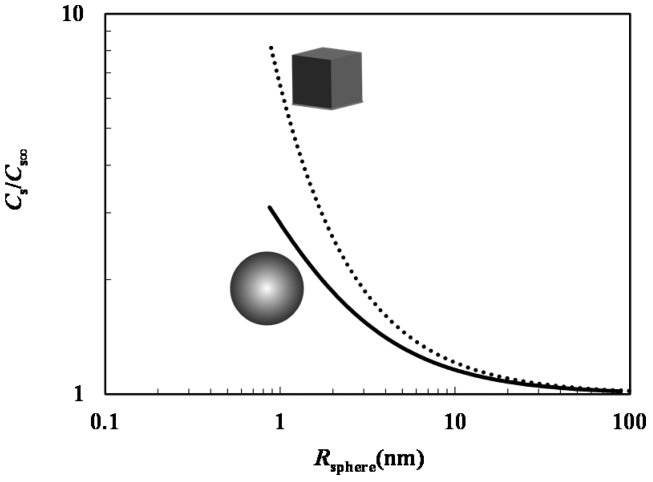

Figure 10. Effect of nanocrystals geometry (sphere, cube ($\xi = \beta = 1$) on the ratio between the solubility of nimesulide nanocrystals (C_s) and that of the infinitely large nimesulide crystal ($C_{s\infty}$) assuming the nanocrystals mass fraction X_{nc} = 1. R_{sphere} is the radius of a sphere sharing the same volume of the cubic nanocrystals. The simulation is arrested at the value corresponding to the nimesulide unit cell volume (2.77 nm^3), i.e., R_{sphere} = 0.87 nm.

(X_{nc} = 1) versus nanocrystals size up to NIM unit cell volume (2.77 nm^3), a value corresponding to R_{sphere} = 0.87 nm. Figure 10, based, for the sake of simplicity, on the assumption that γ_d is almost constant with concentration, allows evaluating the ratio $C_s/C_{s\infty}$, where $C_{s\infty}$ is the mass/volume solubility of the infinitely large NIM crystal. The choice of the cubic shape is dictated by the approximately cubic morphology of the real NIM nanocrystals as predicted by the WinXMorph software.[68] It is clear that the cubic shape implies a more pronounced increase of solubility since cubic crystals are characterized by lower T_m and ΔH_m with respect to spherical crystals of the same volume (see Figure 8). Interestingly, the maximum theoretical solubility increase occurring for $R_{sphere} \rightarrow 0.87$ nm (approximately 8-fold), is compatible with the solubility increase of amorphous drugs (not chemically too dissimilar to NIM) lying in the range 10−100 (the amorphous drug is expected to be more soluble than the nanocrystalline drug).[70,71]

On the basis of the previously provided evidence and with the aim of validating the trends predicted by the presented thermodynamic model, MD calculations were performed to derive T_m and ΔH_m behavior of parallelepiped-shaped nanocrystals as a function of selected shape factors (ξ = 0.1, 1, 10) for three small organic drugs. Figure 11 shows the comparison

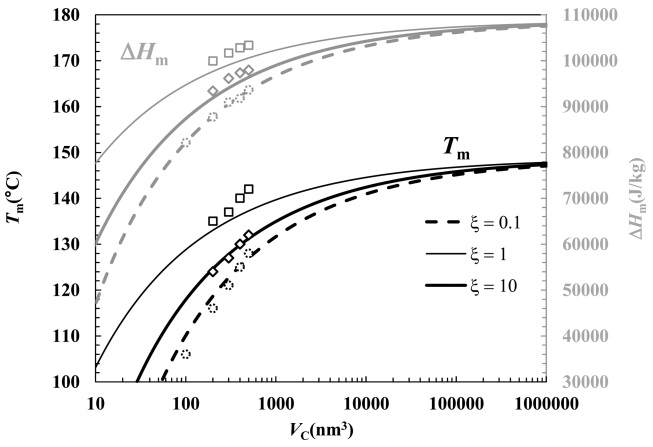

Figure 11. Comparison between the melting temperature T_m (left vertical axis) and enthalpy ΔH_m (right vertical axis) decrease according to the thermodynamic model (eqs 9 and 10); solid black and gray lines, respectively) and to the molecular dynamics approach (symbols). The simulations were performed assuming nimesulide nanocrystals in the form of parallelepipeds characterized by a square base (β = 1), three different values of the shape factor (ξ = 0.1, 1, 10) and the nanocrystals mass fraction X_{nc} = 1.

between the T_m and ΔH_m reduction predicted by the thermodynamic model (eqs 9 and 10, continuous lines) with that obtained by the MD approach (open symbols). MD calculations confirm the decrease in T_m and ΔH_m as a function of nanocrystal volume envisaged by the thermodynamic model. In addition, the influence of the shape ratio (ξ) at constant crystal volume is properly resolved.

A further verification of the model was performed by considering two other small organic drugs (nifedipine and griseofulvin, whose characteristics are reported in Supporting Information, Table S1 and Table S2, respectively), always belonging to the Amidon class II (low water solubility and good permeability). Figures S1−S4 (see Supporting Information) show that a reasonable agreement between model predictions and MD simulations was achieved also for NIF and GRI.

CONCLUSIONS

The thermodynamic model developed in this paper allows evaluating the effect of size and shape on T_m and ΔH_m of organic (drug) nanocrystals. In particular, the differences existing among spherical, cylindrical, and parallelepiped-shaped nanocrystals, characterized by different shape ratios (from needles to platelets), are explained in terms of the ratio between the number of surface and bulk molecules. Indeed, the higher this ratio, the higher the T_m and ΔH_m reductions are and, consequently, the higher the drug solubility is. As solubility increase is reflected in drug bioavailability enhancement, the considerable practical effect of nanocrystals geometry on nanocrystals based delivery systems clearly emerges.

Model reliability, tested in the case of a well-known poorly water-soluble drug (nimesulide, a nonsteroidal anti-inflammatory drug), is supported by the fact that the predicted solubility increase is physically sound in relation to the solubility of the amorphous drug, which is expected to be considerably higher. In addition, our model reliability was also proved by the results obtained from an MD approach, which confirms the T_m and ΔH_m reduction predicted by the thermodynamic model and the effect of shape ratio variation. Accordingly, this model may be considered a reliable tool for the characterization/design of nanocrystals based delivery systems (determination of X_{nc} and nanocrystals size distribution in polymer-drug systems) and for the evaluation of nanocrystals solubility increase, an aspect of paramount importance for the bioavailability enhancement of poorly water-soluble drugs. In addition, as it relies on thermodynamics, the developed model potentially holds for every drug and their polymorphic forms which may be considerably significant in the pharmaceutical field. Clearly, it requires the knowledge of a certain number of fundamental physical parameters such as surface tension, density, and $T_{m\infty}$/$\Delta H_{m\infty}$ of the specific drug/polymorphic species.

Finally, the presented model constitutes the starting point for the development of a thermodynamic model able to consider the actual shape of drug nanocrystals (typically appearing in form of complex prisms) and the possible variation of surface energy on the distinct crystal facets.

ASSOCIATED CONTENT

Tables S1−S2 and Figures S1−S4 showing the comparison between the developed thermodynamic model and the MD approach for other the two poorly soluble drugs: nifedipine and griseofulvin; Appendix (PDF)

Nimesulide-melting AVI file showing the melting process of nimesulide crystals as detected by hot stage microscopy (AVI)

AUTHOR INFORMATION

Corresponding Author

*Address: Department of Engineering and Architecture (DIA), Trieste University, Via Alfonso Valerio, 6/A, I 34127 Trieste, Italy. E-mail: mario.grassi@dia.units.it. Fax: 0039-040-569823. Tel: 0039-040-5583435.

ORCID

Paola Posocco: 0000-0001-8129-1572

Sabrina Pricl: 0000-0001-8380-4474
Mario Grassi: 0000-0002-3532-3200

Notes

The authors declare no competing financial interest.

■ ACKNOWLEDGMENTS

M.G. wishes to thank Prof. Elena Boldyreva for helpful discussions. This work has been supported by the Italian Minister of Instruction, University and Research (MIUR), PRIN 2010-11, [20109PLMH2], and by the "Fondazione Beneficentia Stiftung" Vaduz.

■ REFERENCES

(1) Grassi, M.; Grassi, G.; Lapasin, R.; Colombo, I. *Understanding Drug Release and Absorption Mechanisms: A Physical and Mathematical Approach*; CRC Press: Boca Raton, 2007.
(2) Lipinski, C. *Am. Pharm. Rev.* **2002**, *5*, 82−85.
(3) Cooper, E. R. *J. Controlled Release* **2010**, *141*, 300−302.
(4) Brun, M.; Lallemand, A.; Quinson, J. F.; Eyraud, C. *J. Chim. Phys. Phys.-Chim. Biol.* **1973**, *70*, 979−989.
(5) Lubashenko, V. V. *J. Nanopart. Res.* **2010**, *12*, 1837−1844.
(6) Huang, W. J.; Sun, R.; Tao, J.; Menard, L. D.; Nuzzo, R. G.; Zuo, J. M. *Nat. Mater.* **2008**, *7*, 308−313.
(7) Toledano, J.-C.; Toledano, P. *The Landau theory of Phase Transitions*; World Scientific: Singapore, 1987.
(8) Jiang, Q.; Shi, H. X.; Zhao, M. *J. Chem. Phys.* **1999**, *111*, 2176−2180.
(9) Zhang, M.; Efremov, M. Y.; Schiettekatte, F.; Olson, E. A.; Kwan, A. T.; Lai, S. L.; Wisleder, T.; Greene, J. E.; Allen, L. H. *Phys. Rev. B: Condens. Matter Mater. Phys.* **2000**, *62*, 10548−10557.
(10) Buckton, G.; Beezer, A. E. *Int. J. Pharm.* **1992**, *82*, R7−R10.
(11) Mosharraf, M.; Nyström, C. *Drug Dev. Ind. Pharm.* **2003**, *29*, 603−622.
(12) Madras, G.; McCoy, B. J. *Cryst. Growth Des.* **2003**, *3*, 981−990.
(13) Carli, F.; Colombo, I.; Magarotto, L.; Motta, A.; Torricelli, C. *Int. J. Pharm.* **1986**, *33*, 115−124.
(14) Grassi, M.; Colombo, I.; Lapasin, R. *J. Controlled Release* **2000**, *68*, 97−113.
(15) Debenedetti, P. G.; Tom, J. W.; Sang-Do, Y.; Gio-Bin, L. *J. Controlled Release* **1993**, *24*, 27−44.
(16) Kikic, I.; Lora, M.; Cortesi, A.; Sist, P. *Fluid Phase Equilib.* **1999**, *158−160*, 913−921.
(17) Grassi, M.; Colombo, I.; Carli, F.; Lapasin, R. *Eur. J. Pharm. Sci.* **1998**, *6*, S65.
(18) Voinovich, D.; Perissutti, B.; Grassi, M.; Passerini, N.; Bigotto, A. *J. Pharm. Sci.* **2009**, *98*, 4119−4129.
(19) Hasa, D.; Voinovich, D.; Perissutti, B.; Bonifacio, A.; Grassi, M.; Franceschinis, E.; Dall'Acqua, S.; Speh, M.; Plavec, J.; Invernizzi, S. *J. Pharm. Sci.* **2011**, *100*, 915−932.
(20) Hasa, D.; Perissutti, B.; Chierotti, M. R.; Gobetto, R.; Grabnar, I.; Bonifacio, A.; Dall'Acqua, S.; Invernizzi, S.; Voinovich, D. *Int. J. Pharm.* **2012**, *436*, 41−57.
(21) Coceani, N.; Magarotto, L.; Ceschia, D.; Colombo, I.; Grassi, M. *Chem. Eng. Sci.* **2012**, *71*, 345−355.
(22) Crowley, K. J.; Zografi, G. *J. Pharm. Sci.* **2002**, *91*, 492−507.
(23) Colombo, I.; Grassi, G.; Grassi, M. *J. Pharm. Sci.* **2009**, *98*, 3961−3986.
(24) Meriani, F.; Coceani, N.; Sirotti, C.; Voinovich, D.; Grassi, M. *J. Pharm. Sci.* **2004**, *93*, 540−552.
(25) Amidon, G. L.; Lennernäs, H.; Shah, V. P.; Crison, J. R. *Pharm. Res.* **1995**, *12*, 413−420.
(26) Nanda, K. K. *Pramana* **2009**, *72*, 617−628.
(27) Goswami, G. K.; Nanda, K. K. *Curr. Nanosci.* **2012**, *8*, 305−311.
(28) Ha, J. M.; Wolf, J. H.; Hillmyer, M. A.; Ward, M. D. *J. Am. Chem. Soc.* **2004**, *126*, 3382−3383.
(29) Ha, J. M.; Hillmyer, M. A.; Ward, M. D. *J. Phys. Chem. B* **2005**, *109*, 1392−1395.
(30) Hamilton, B. D.; Ha, J. M.; Hillmyer, M. A.; Ward, M. D. *Acc. Chem. Res.* **2012**, *45*, 414−423.
(31) Zandavi, S. H.; Ward, C. A. *J. Colloid Interface Sci.* **2013**, *407*, 255−264.
(32) Beiner, M.; Rengarajan, G. T.; Pankaj, S.; Enke, D.; Steinhart, M. *Nano Lett.* **2007**, *7*, 1381−1385.
(33) Rengarajan, G. T.; Enke, D.; Steinhart, M.; Beiner, M. *J. Mater. Chem.* **2008**, *18*, 2537−2539.
(34) Hasa, D.; Miniussi, E.; Jones, W. *Cryst. Growth Des.* **2016**, *16*, 4582−4588.
(35) Belenguer, A. M.; Lampronti, G. I.; Cruz-Cabeza, A. J.; Hunter, C. A.; Sanders, J. K. M. *Chem. Sci.* **2016**, *7*, 6617−6627.
(36) Lee, S. Y.; Yu, G.; Shin, K.; Kim, I. W. *J. Nanosci. Nanotechnol.* **2013**, *13*, 2348−2353.
(37) Graubner, G.; Rengarajan, G. T.; Anders, N.; Sonnenberger, N.; Enke, D.; Beiner, M.; Steinhart, M. *Cryst. Growth Des.* **2014**, *14*, 78−86.
(38) Sonnenberger, N.; Anders, N.; Golitsyn, Y.; Steinhart, M.; Enke, D.; Saalwächter, K.; Beiner, M. *Chem. Commun.* **2016**, *52*, 4466−4469.
(39) Eral, H. B.; López-Mejías, V.; O'Mahony, M.; Trout, B. L.; Myerson, A. S.; Doyle, P. S. *Cryst. Growth Des.* **2014**, *14*, 2073−2082.
(40) Badruddoza, A. Z. M.; Godfrin, P. D.; Myerson, A. S.; Bernhardt, L.; Trout, B. L.; Doyle, P. S. *Adv. Healthcare Mater.* **2016**, *5*, 1960−1968.
(41) O'Mahony, M.; Leung, A. K.; Ferguson, S.; Trout, B. L.; Allan, S.; Myerson, A. S. *Org. Process Res. Dev.* **2015**, *19*, 1109−1118.
(42) Dwyer, L.; Kulkarni, S.; Ruelas, L.; Myerson, A. S. *Crystals* **2017**, *7*, 131.
(43) Davis, R.; Brogden, R. N. *Drugs* **1994**, *48*, 431−454.
(44) Pawlow, P. Z. *Z. Phys. Chem.* **1909**, *65*, 1−35.
(45) Sdobnyakov, N. Y.; Samsonov, V. M.; Bazulev, A. N.; Kul'pin, D. A. *Bull. Russ. Acad. Sci.: Phys.* **2008**, *72*, 1371−1373.
(46) Bergese, P.; Colombo, I.; Gervasoni, D.; Depero, L. E. *J. Phys. Chem. B* **2004**, *108*, 15488−15493.
(47) Bergese, P.; Alessandri, I.; Colombo, I.; Coceani, N.; Depero, L. E. *Composites, Part A* **2005**, *36*, 443−448.
(48) Hasa, D.; Voinovich, D.; Perissutti, B.; Grassi, G.; Fiorentino, S. M.; Farra, R.; Abrami, M.; Colombo, I.; Grassi, M. *Eur. J. Pharm. Sci.* **2013**, *50*, 17−28.
(49) Hasa, D.; Perissutti, B.; Voinovich, D.; Abrami, M.; Farra, R.; Fiorentino, S. M.; Grassi, G.; Grassi, M. *Chem. Biochem. Eng. Q.* **2014**, *28*, 247−258.
(50) Adamson, A. W.; Gast, A. P. *Physical Chemistry of Surfaces*, 6th ed.; Wiley-Interscience: New York, 1997.
(51) Gibbs, J. W. *The Collected Works of J. Willard Gibbs*; Yale University Press: New Haven, 1928.
(52) Sar, D. K.; Nayak, P.; Nanda, K. K. *Phys. Lett. A* **2008**, *372*, 4627−4629.
(53) Heng, J. Y. Y.; Bismarck, A.; Lee, A. F.; Wilson, K.; Williams, D. R. *Langmuir* **2006**, *22*, 2760−2769.
(54) Tolman, R. C. *J. Chem. Phys.* **1949**, *17*, 333−337.
(55) Samsonov, V. M.; Sdobnyakov, N. Y.; Bazulev, A. N. *Colloids Surf., A* **2004**, *239*, 113−117.
(56) Lu, H. M.; Wen, Z.; Jiang, Q. J. *J. Phys. Org. Chem.* **2007**, *20*, 236−240.
(57) Jiang, Q.; Shi, H. X.; Zhao, M. *Acta Mater.* **1999**, *47*, 2109−2112.
(58) Rowlinson, J. S.; Windom, B. *Molecular Theory of Capillarity*; Clarendon Press: Oxford, 1982.
(59) Groom, C. R.; Bruno, I. J.; Lightfoot, M. P.; Ward, S. C. *Acta Crystallogr., Sect. B: Struct. Sci., Cryst. Eng. Mater.* **2016**, *72*, 171−179.
(60) Bayly, C. I.; Cieplak, P.; Cornell, W.; Kollman, P. A. *J. Phys. Chem.* **1993**, *97*, 10269−10280.
(61) Sanphui, P.; Sarma, B.; Nangia, A. *J. Pharm. Sci.* **2011**, *100*, 2287−2299.
(62) Berendsen, H. J. C.; Postma, J. P. M.; van Gunsteren, W. F.; DiNola, A.; Haak, J. R. J. *J. Chem. Phys.* **1984**, *81*, 3684−3690.
(63) Kumar, D.; Shastri, N. R. *Cryst. Growth Des.* **2014**, *14*, 326−338.

(64) Zhu, W.; Romanski, F. S.; Dalvi, S. V.; Dave, R. N.; Tomassone, M. S. *Chem. Eng. Sci.* **2012**, *73*, 218−230.
(65) Grassi, M.; Coceani, N.; Magarotto, L. *Int. J. Pharm.* **2002**, *239*, 157−169.
(66) Magomedov, M. N. *Phys. Solid State* **2004**, *46*, 954−968.
(67) Magomedov, M. N. *Tech. Phys.* **2011**, *56*, 1277−1282.
(68) Kaminsky, W. *J. Appl. Crystallogr.* **2007**, *40*, 382−385.
(69) Hasa, D.; Giacobbe, C.; Perissutti, B.; Voinovich, D.; Grassi, M.; Cervellino, A.; Masciocchi, N.; Guagliardi, A. *Mol. Pharmaceutics* **2016**, *13*, 3034−3042.
(70) Murdande, S. B.; Pikal, M. J.; Shanker, R. M.; Bogner, R. H. *J. Pharm. Sci.* **2010**, *99*, 1254−1264.
(71) Bahl, D.; Bogner, R. H. *Pharm. Res.* **2006**, *23*, 2317−2325.